Article:
Li, Y., Kumari, P. and Boston, R. (2026) Improving conductivity in Na2Ti3O7 for Na-Ion anodes through Ti reduction. Journal of The Electrochemical Society, 173 (8). 080505. ISSN: 0013-4651

https://doi.org/10.1149/1945-7111/ae58fb

Journal of The
Electrochemical Society

Improving Conductivity in $Na_2Ti_3O_7$ for Na-Ion Anodes through Ti Reduction

To cite this article: Yining Li *et al* 2026 *J. Electrochem. Soc.* **173** 080505

Journal of The Electrochemical Society, 2026 **173** 080505

Improving Conductivity in $Na_2Ti_3O_7$ for Na-Ion Anodes through Ti Reduction

Yining Li, Pooja Kumari, and Rebecca Boston[z]

School of Chemical, Materials, and Biological Engineering, Sir Robert Hadfield Building, University of Sheffield, S1 3JD, United Kingdom

$Na_2Ti_3O_7$ is a promising anode material for use in sodium ion batteries, however it suffers from low total conductivity, which is critical for conversion anode performance. Here we employ a reduction strategy, removing oxygen from the crystal structure during synthesis, aiming to increase the total conductivity through reduction of Ti ions. Using impedance spectroscopy, we show that the room temperature conductivity can be increased from 9.7×10^{-8} S.cm^{-1} to 4.0×10^{-7} S.cm^{-1} in the reduced NTO. Using cyclic voltammetry, we show that the reduced material shows a modest increase in specific capacity and rate capability, which we attribute to improved sodium ion mobility due to wider Na-ion channels, and decreased activation energy (170 meV in the reduced sample vs 250 meV at room temperature). This demonstrates that using reduction during synthesis is a viable method to simultaneously improve multiple key electrochemical properties in $Na_2Ti_3O_7$.

 [DOI: 10.1149/1945-7111/ae58fb]

Manuscript submitted February 16, 2026; revised manuscript received March 25, 2026. Published April 17, 2026.

Supplementary material for this article is available online

As demand for Li-ion batteries increases, sodium ion batteries have become a leading candidate to supplement Li-ion technologies in some applications. Substantial research into the materials required for competitive Na-ion batteries has already been conducted, although much of this has focused on cathode materials, such as layered transition metal oxides. The anode side has had comparatively less attention, however, there remain a number of challenges to be solved on the anode side, before the promise of Na-ion cells can be fully realised.

There are a number of active research directions for anode materials,[1] including hard carbons,[2–4] alloying materials,[5] iron sulphides[6] and sodium titanates.[7,8] The sodium titanate family of materials are most commonly studied as the $Na_2Ti_3O_7$ or $Na_2Ti_6O_{13}$ phases,[1] with the $Na_2Ti_3O_7$ phase showing high specific capacity (theoretical capacity up to 178 mAh g^{-1})[8] but generally low capacity retention over long-term cycling,[9,10] whereas $Na_2Ti_6O_{13}$ has low capacity but good stability.[11] A number of studies have also demonstrated that anodes comprising both of these phases share the benefits of both, retaining the high specific capacity whilst preserving cycle stability.[12,13] Titanates are of particular interest for anodes due to their low voltage plateau (0.3 V vs Na/Na$^+$ in $Na_2Ti_3O_7$),[14] high elemental abundance, and relatively low cost.[1,15]

Whilst successful, their electronic conductivity remains intrinsically low, primarily due to their wide bandgap and the lack of free charge carriers.[16] This limitation is reflected in the relatively large activation energies observed. One study reported this as 0.79 eV for $Na_2Ti_3O_7$,[17] and another at 0.68 eV.[18] The room-temperature conductivity can be inferred from this second study to be in the range of 10^{-7} to 10^{-8} S cm^{-1}, with Arrhenius-type behaviour in the low-temperature range (–40 °C to 120 °C).[18]

In order to increase the electrical conductivity of titanates, previous studies have sought to alter the oxidation state of the titanium ions in the lattice. Numerous studies on perovskite titanates such as doped strontium titanates[19,20] and barium titanate[21] have taken the approach of reducing some of the titanium ions within the lattice during synthesis. This is achieved by synthesising (or sintering) the material under flowing hydrogen (usually as a mixture of 5% H_2/95% N_2, the low level of hydrogen chosen for practical and safety reasons). This results in reduction of some of the titanium ions through removal of oxygen from the lattice (lost as H_2O), as described in Eq. 1. Each oxygen lost generates two additional electrons in the lattice, one which combines with a d^0 Ti ion to form a d^1 Ti ion, generating a change in colour (white to black)[22] and increase in electrical conductivity.

$$H_2 + O_O^x \rightarrow V_O^{\cdot\cdot} + 2e^- + H_2O \quad [1]$$

In previous studies, this has resulted in measured increases in the electrical conductivity. Examples include $Sm_{0.15}Sr_{0.85}TiO_3$, where the electrical conductivity at 50 °C increases from around 120 S.cm^{-1} in an unreduced sample to around 1250 S.cm^{-1} once reduced in H_2/N_2.[23] Similarly, oxygen partial pressure was used to control degree of reduction in rare Earth doped $SrTiO_3$, showing modest increases in conductivity as a result.[24] These types of reduced samples have been used as a strategy alongside other vacancy approaches to improve e.g. thermoelectric properties in *n*-type ceramics.[19]

This type of approach has also been demonstrated in Na-ion anode materials. One study introduced oxygen vacancies into anatase TiO_2 via $NaBH_4$ reduction.[25] XPS analysis confirmed the presence of Ti^{3+}, which enhanced electronic conductivity. CV measurements revealed that the oxygen-deficient TiO_2 exhibited more stable redox peaks at 0.69 V (reduction) and 0.83 V (oxidation) compared to pristine anatase TiO_2, with a reduced peak separation ($\Delta V = 0.14$ V vs 0.27 V), indicating improved reaction reversibility. Moreover, their oxygen deficient TiO_2 retained 91.2 mAh.g^{-1} at a rate of 20 C, outperforming pristine anatase TiO_2 by 2.5 times. In a subsequent study, the same group incorporated high-concentration phosphorus doping (~7.8 at.%) into oxygen-deficient TiO_2.[26] The phosphorus atoms replaced unstable Ti^{3+} sites, further optimizing the material's electronic structure. At an ultra-high rate of 10 A g^{-1}, the material still maintained a reversible capacity of 167 mAh.g^{-1}. This demonstrated that oxygen vacancies reduced the TiO_2 band gap from 3.26 eV to 3.15 eV, while the presence of Ti^{3+} improved electronic conductivity and facilitated Na^+ migration, enabling ultrafast charge-discharge capability.[26]

Previous studies have demonstrated that introducing Ti^{3+} can enhance the electronic conductivity and electrochemical performance of $Na_2Ti_3O_7$. Meng et al.[27] also developed a complex hollow NTO/C(N) composite system, with a chemically bonded interface, combining vacancy engineering with heteroatom doping to achieve excellent long-term and low-temperature performance. They enabled 80,000-cycle stability at 5 A.g^{-1} and 59 mAh.g^{-1} at 20 A.g^{-1}. The improved performance is attributed to bandgap narrowing and increased charge carrier density introduced by Ti^{3+}. In addition,

[z]E-mail: r.boston@sheffield.ac.uk

the larger ionic radius of Ti^{3+} induces lattice expansion, facilitating Na^+ diffusion and enhancing rate capability.

Song et al.[28] employed a post-treatment in 5% H_2/Ar to generate self-doped Ti^{3+} and applied carbon coating, resulting in improved rate capability and cycling stability. They used a modified sol gel synthesis method to generate carbon-$Na_2Ti_3O_7$ composite powders, with an anneal in a H_2 environment. They show a four-fold improvement in conductivity on powders using a four-pole method, from 0.0665 S.cm^{-1} in non-reduced materials to 0.249 S.cm^{-1} in the reduced samples. The conductivity reported in the non-reduced sample here is well in excess of the values reported elsewhere (without carbon),[18] and so it is highly likely that the additional carbon is providing additional pathways for electron conduction, rather than these values being indicative of the conductivity of the $Na_2Ti_3O_7$ itself.[28] Electrochemical impedance spectroscopy is also explored; however, the paper stops short of measuring the activation energy. This is also reflected in the values of specific capacity reported, which are very high on first cycle, attributed to the carbon present, and settle at around 100 mAh.g^{-1} after 100 cycles at 0.1 C, which is also likely to be due to some capacity within the carbon itself. This therefore leaves significant scope for understanding the intrinsic material properties of the reduced material in its phase pure (i.e. no added carbon) form.

Here we seek to understand the properties of reduced $Na_2Ti_3O_7$ alone, using powders made in-house using solid state processing, and the H_2/N_2 reduction approach, and compare these to the non-reduced powder. We sinter dense pellets for impedance spectroscopy, and investigate the electrochemical properties of both the as-synthesised powders, and powders re-formed from the sintered pellets, to ensure that the material in the pellets is genuinely representative of the materials used in the batteries formed, despite the differing thermal history. We demonstrate a four-fold increase in conductivity, and modest improvements in the electrochemical properties, without needing to form a carbon composite.

Methods

Sample preparation.—$Na_2Ti_3O_7$ powders were synthesised using standard solid state synthesis methods. Briefly, stoichiometric quantities of titanium dioxide (99.5% purity, Sigma Aldrich, UK) and sodium carbonate (99.5% purity, ACROS, UK) were dried, batched, and ball milled. Calcination was performed under different conditions: under H_2/N_2 (5%–95%) to produce reduced $Na_2Ti_3O_7$ (hereafter called R-NTO), and in air as a control (hereafter called NTO). All samples were calcined at 800 °C for 10 h, followed by further ball milling

To make sintered pellets, only the NTO powder was pressed using a uniaxial press, for solid state sintering. All pellets were initially sintered at 1050 °C for 8 h in air, with the R-NTO pellets then being created by performing a second anneal step at 800 °C for 12 h in H_2/N_2 to reduce the Ti. Pellets were polished to remove surface impurity phases, leaving sintered samples approximately 8.5 mm in diameter and 1–2 mm thick.

Density of the sintered pellets was measured using an Archimedes density balance (Mettler Toledo, MS104S).

Some pellets were then crushed and milled to create powder for use in half cells. This powder was generated in order to confirm that the sintering process had not significantly altered the electrochemical properties of the materials, ensuring that the impedance tests were representative of the as-calcined powders.

Characterisation.—X-ray diffraction (XRD) on all powder and solid ceramic samples was performed using an PANalytical X'Pert^3 diffractometer, using Cu k-alpha radiation. Rietveld refinement was performed using GSAS II,[29] refining lattice parameters, peak shape parameters (Caglioti W, V, U and asymmetric factors X, Y, Z), atomic positions and occupancies (following the order of high to low scattering factors: Na, Ti and O), thermal parameters (in order of high to low scattering factors), and instrument parameters.

Samples for scanning electron microscopy (SEM) were affixed to double-sided carbon stickers and coated with a thin layer of gold before imaging using an Inspect F (FEI) SEM.

Impedance spectroscopy was performed on the sintered, gold-coated pellets using an Agilent E4980A Precision LCR Meter between 23 °C and 400 °C using a frequency range of 0.02 Hz–1 MHz, with an applied voltage of 100 mV. Tests were performed under argon to protect against re-oxidation of the reduced samples. Analysis of impedance spectroscopy data included a correction for the geometry of the pellet.

Battery preparation.—Half cells were prepared using the R-NTO and NTO calcined powders, and as further controls, the sintered pellets which were then crushed back into powder were also prepared as half cells. A ratio of 7:2:1 (w/w) of active material: conductive material: binder was used throughout.

Active materials were dried in a vacuum oven (120 °C) overnight before slurry preparation, along with the conductive carbon (Timical Super C65, MTI) and binder (Polyvinylidene fluoride, PVDF, MTI) at 80 °C.

To prepare half cells, 1.5 mL of N-methyl-2-pyrrolidone (NMP, 99.5%, Sigma Aldrich), was added to 0.05 g PVDF in an Ar-filled glovebox and combined using a Thinkymixer (Thinky). Next, 0.1 g C65 and 0.35 g active material were hand ground together using a pestle and mortar. The mixed powder was added to the PVDF-NMP mixture, along with an additional c.0.5 ml NMP. The resulting mixture then was fully homogenised using the Thinkymixer: slurries were mixed at 2000 rpm for 2.5 min, followed by defoaming for 30 s at 2200 rpm, with these two steps repeated six times.

Slurry was then cast onto a carbon coated aluminium foil (MTI) using a draw down table with a thickness of 250 μm. After drying, the slurry was calendared to approximately 50% of its original thickness before being punched into discs (diameter = 12 mm). The average mass of the discs was 0.11 g (including the carbon-coated film as 0.05 g), indicating an active material loading of approximately 3.17 mg cm^{-2}.

Cells were assembled in stainless steel 2032 coin cell casing (MTI). The counter electrode was made from sodium metal, cut into a disc (diameter = 10 mm, 99.8%, Alfa Aesar), and was also used as the reference electrode during cycling. Separators were punched from a glass microfiber sheet (Whatman GF/6) and soaked in 100 μl of commercial Kishida electrolyte (1 M $NaPF_6$ in ethylene carbonate:diethyl carbonate 1:1, Kishida) during assembly. A gas driven crimper (MTI) was used to seal the cells.

For galvanostatic cycling measurements, each material was tested at 0.05 C and 0.1 C. All batteries started with a 6 h rest period, and a 10 min rest was applied between each charge and discharge step. The voltage window was set from 0.01 V to 2.5 V for all cells for 100 cycles, using the Neware Battery Testing System (BTS). The rate performance test was also conducted using the Neware Battery Testing System, with C rate of 0.05 C, 0.1 C, 0.5 C, 1 C, and 2 C for eight cycles each. The temperature of the cycle test system was set up at 25 °C by a temperature control chamber (ECO HTCL 400, TAS).

A Macor Series 4300 Battery Cycler (MACCOR, Inc.) was used for cyclic voltammetry (CV). CV data was collected between the cut-off voltages of 0.0 V and 3.0 V (vs Na^+/Na) at a scan rate of 0.08 mV s^{-1}. For all cycling data presented, at least three repeats were performed, with representative data from a single cell presented.

Results and Discussion

X-ray diffraction was used to confirm phase formation of NTO powder (Fig. 1a) and R-NTO powder (Fig. 1b). Rietveld refinement was used to calculate lattice parameters and occupancies of all three elements. X-rays are not the most sensitive probe of oxygen however the occupancies were calculated as indicative values. Table I gives the refinement values for the two samples. The lattice parameters of

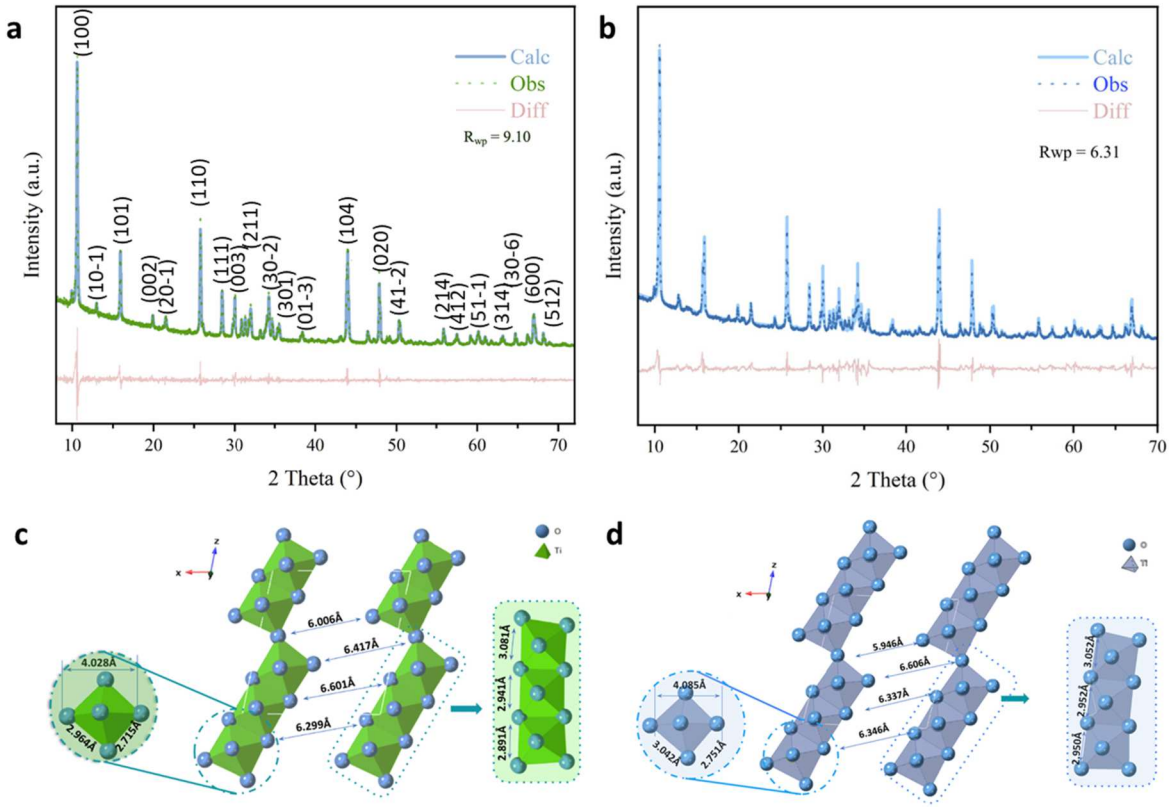

Figure 1. X-ray diffraction and Rietveld analysis fits of (a) the non-reduced NTO including indexed peaks and (b) the reduced sample, R-NTO. Rietveld refinement parameters can be found in Table I. The crystal structures generated from the refinements are shown in (c) for the NTO and (d) for R-NTO. Note the increase in channel width from the unreduced to the reduced sample, which might aid Na ion mobility.

Table I. Refinement parameters of NTO and R-NTO.

	NTO	R-NTO
a (Å)	8.5601 (5)	8.5625 (4)
b (Å)	3.8007 (3)	3.8014 (3)
c (Å)	9.1239 (6)	9.1258 (5)
O occupancy	6.53 (5)	6.32 (5)
Na Biso ($Å^2$)	1.235 ± 0.127	1.534 ± 0.250
Ti Biso ($Å^2$)	0.510 ± 0.179	0.713 ± 0.199
O Biso ($Å^2$)	1.209 ± 0.416	1.432 ± 0.300
Rwp	9.10 (3)	6.31 (4)
β (°)	101.5951 (8)	101.5865 (8)
Colour	White	Grey

R-NTO increase vs the non-reduced powder, with notable increases in the *a* and *c* parameters, and a smaller increase in *b*, as shown in Table I and Figs. 1c and 1d. This is attributed to the larger ionic radius of Ti^{3+} vs Ti^{4+}, the presence of which is confirmed by both a change in colour of the sample (from white Ti^{4+}, to black Ti^{3+}, Figs. 2a and 2b), and a change in oxygen occupancy from 6.53(5) to 6.32(5).

Additionally, the refinement shows that the layer spacing between the Ti octahedra, and in particular the O1-O6 distance, increases in R-NTO vs NTO, Figs. 1c and 1d. Given that these are the channels through which the Na ions move during cycling, this may lead to improvements in Na ion mobility.[30,31]

Half cells were fabricated using the procedure outlined in the methods section, and cycled between 0.01 V and 2.5 V for 100 cycles. Comparison of the specific capacities and coulombic efficiencies of the NTO and RNTO are shown in Fig. 3a.

Initial capacity for the R-NTO samples was significantly higher than the non-reduced NTO sample. Both samples lose capacity over the first few cycles, as has been described previously (the origin of the large first cycle losses is still unclear). Interestingly, the initial losses in the RNTO sample occur over a larger number of cycles than the NTO sample potentially indicating a different surface mechanism. Given the similarity in particle size and morphology between two powders (Fig. 2c and 2d) this is unlikely to be the driver for the differences observed. Following these initial losses, the RNTO capacity remains consistently higher than the NTO cells through to 100 cycles, retaining 94 $mAh.g^{-1}$ vs 83 $mAh.g^{-1}$

Rate performance tests were conducted to evaluate the electrochemical performance of the materials at different charge-discharge rates, as shown in Fig. 3b. No significant differences were observed between R-NTO and NTO at the low rate, however as the C-rate was increased, R-NTO showed higher specific capacity. Across the entire range of C-rates, R-NTO consistently outperformed NTO, which we attribute to the likely enhanced Na^+ diffusion rates enabled by the slight increase in Na channel width (Figs. 1c and 1d). In contrast, NTO suffers from more severe capacity fading at high rates due to poorer conductivity and limited ion diffusion. Specific charge and discharge profiles are given for these 100 cycles (Figs. 3c–3f), showing similar voltage profiles across both samples.

Cyclic voltammetry (CV, Fig. 4) was performed, using a scan rate of 0.08 $mV.s^{-1}$ within a voltage range of 0.0–3.0 V to investigate the sodium storage mechanism. For both types of cell, during the first sodium ion insertion, the reduction reaction began at 1.1 V and formed a strong peak at 0.3 V. This indicates that the reduction reaction of the electrolyte primarily started at this voltage. This broad peak did not reappear in subsequent scans for either R-NTO and NTO, further confirming that the SEI layer was irreversibly formed from around 0.7 V during the initial cycle, although the impact of this on specific capacity is more substantial in the non-reduced sample.

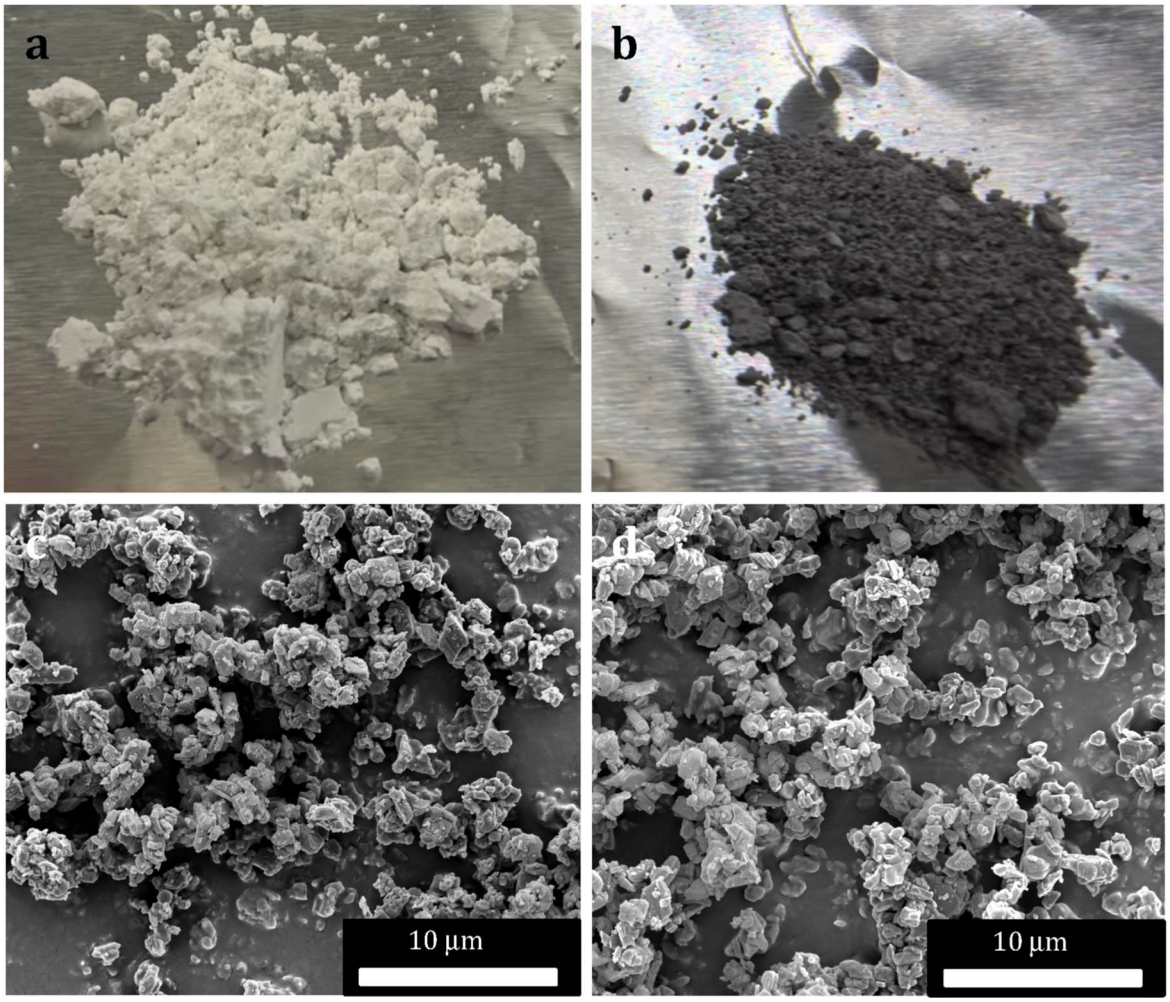

Figure 2. Images of (a) the white non-reduced NTO, and (b) the dark grey reduced R-NTO. Corresponding representative SEM images of (c) the non-reduced powder, and (d) the RNTO powder, showing no discernible change in size or morphology between the two samples.

The similar electrochemical performance of the two materials provides strong evidence that there is no significant difference in their charge and discharge principles. This finding aligns with the conclusion regarding the similarity in their crystal structures and morphologies. During the first 20 cycles, a stable anodic peak at 0.03 V was observed in both types of cell, representing the reversible sodium ion insertion into the layer between TiO_6 of $Na_2Ti_3O_7$.[30]

For NTO, Na^+ extraction is indicated by a strong cathodic peak at 0.30–0.40 V. The anodic peak shifts over the 20 cycles, and shoulder peaks appeared during some cycles. This observation suggests some unpredictability in cycling performance of NTO, suggesting significant changes in the electrode material during these cycles, potentially caused by structural expansion or interfacial instability.[32] In contrast, the anodic peak of R-NTO at 0.35 V remained highly stable in both shape and position, indicating that reactions are more stable over multiple cycles. This stability might be attributed to the oxygen vacancies in R-NTO, which enhance ionic conductivity and reduce structural impacts during Na^+ insertion/extraction.[28]

Another shared trend between R-NTO and NTO is that, with increasing charge-discharge cycles (indicated by the colour gradient from dark to light in Fig. 4), the intensity of the anodic peak at c.0.35 V gradually diminished, while a peak at 0.40 V emerged and progressively strengthened. This represents the existence of two distinct Na^+ storage sites in the $Na_2Ti_3O_7$ structure: one at 0.30 V, which is kinetically favourable but energetically less stable, and another at 0.40 V, which is kinetically less favourable but energetically more stable.[33]

Additionally, as cycling progressed, R-NTO showed a faster emergence and stabilisation of the 0.48 V site more quickly than NTO. This is a minor structural transition, and the site is known to be a stable region, exhibits lower internal stress and a more stable lattice structure,[33] which effectively buffers volume expansion/contraction during repeated ion insertion/extraction. This buffering prevents capacity fade caused by lattice distortion and polarisation.

In order to understand the effect of sample reduction on conductivity, pellets of each powder were sintered for testing using impedance spectroscopy. This requires production of sintered pellets, which changes the thermal history of the material, potentially changing other properties such as phase as well. Due to challenges encountered at this stage, the most reliable route to dense, reduced pellets was found to be by sintering the NTO powder to produce a dense pellet, followed by a separate reduction step.

To ensure, therefore, that the pellets tested using impedance spectroscopy were representative of the as-made powders used in the half cells, full characterisation of the pellets was undertaken. Initial XRD patterns of the R-NTO pellets indicated formation of a secondary phase ($Na_{0.8}Ti_4O_8$) which was removed by polishing the surface of the pellet (Fig. S1). We attribute this to sodium loss at the surface at high temperatures. XRD of the NTO sample can be seen in Fig. S2 showing no change in phase vs the powder. The surface of the NTO pellets were also polished for consistency. Following this,

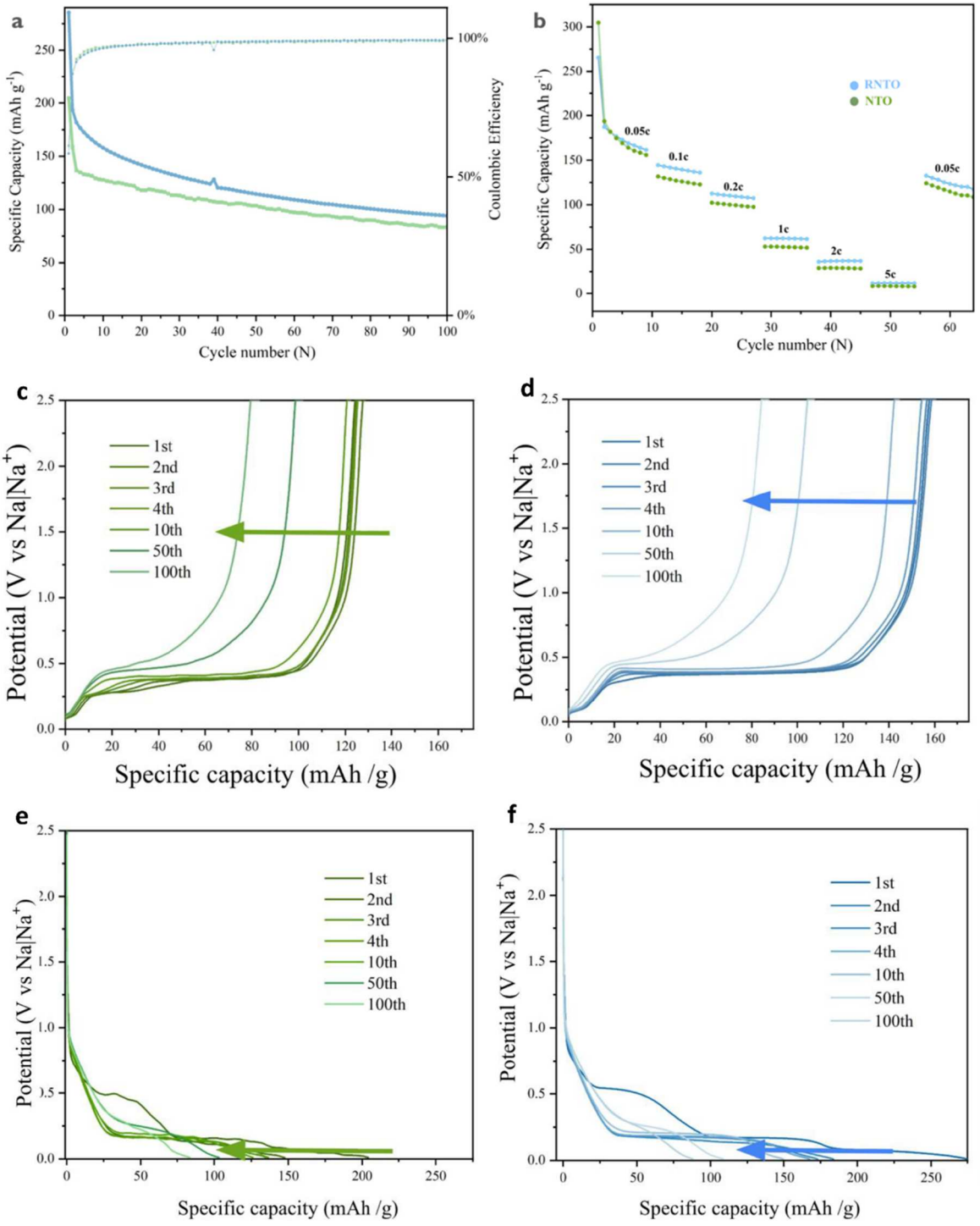

Figure 3. (a) specific capacity and Coulombic efficiency at 0.1 C, and (b) rate capabilities of the two samples, NTO (green) and RNTO (blue). Specific charge (c), (d) and discharge (e), (f) profiles for selected cycles are presented showing similar profiles between NTO (green) and RNTO (blue) samples out to 100 cycles. Arrows in (c)–(f) indicate direction of cycles with increasing cycle number.

both types of pellet were crushed back into powder and prepared as half cells. The resulting specific capacity data are shown in Fig. S3, demonstrating that the pellets are representative of the as-prepared powders. Finally, the densities of the pellets were measured using an Archimedes density balance, and found to be >96% in both cases.

To investigate the intrinsic conductivity of R-NTO and NTO, impedance spectroscopy was conducted over a range of temperatures. Considering that R-NTO is sensitive to oxygen partial pressure and the need for consistency in comparative experiments, all measurements were conducted under an Ar atmosphere. The Nyquist plots of NTO and R-NTO are shown in Figs. 5a and 5b. It is evident that neither R-NTO nor NTO exhibit ideal semicircles, indicating the involvement of more than one component in the conduction process.[34] For NTO (Fig. 5a), most of the curves appear as incomplete semicircles, with some noise at lower temperatures due to the higher resistances. In contrast, RNTO (Fig. 5b) exhibits relatively complete curves at all temperatures. Furthermore, at the same temperature, the estimated intersection of the NTO curve with the real axis (Z') in the low-frequency region (right side) is nearly an order of magnitude larger than that of RNTO. This indicates that the

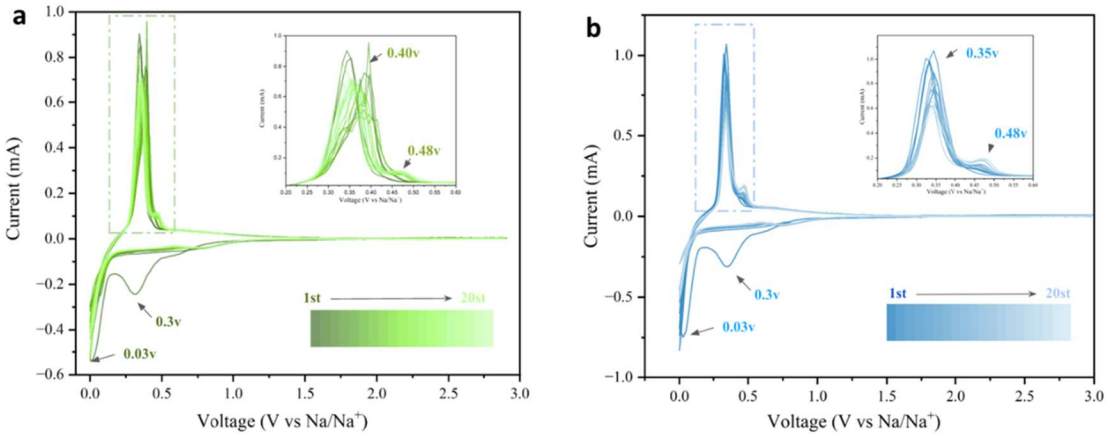

Figure 4. Cyclic voltammetry plots of (a) NTO and (b) R-NTO cells, showing the first 20 cycles (low to high cycle numbers following gradient dark to light). Scans were conducted over a range of 0.0–3.0 V.

total resistance of NTO is significantly higher than that of RNTO. This total resistance reflects the sum of the solution resistance (R_s) and charge transfer resistance (R_{ct}), representing the overall impedance of the material.

The curves of R-NTO and NTO both display combinations of more than one semicircle, due to differing behaviour between the bulk and grain boundary in the samples. This was further confirmed by the capacitance spectra, which exhibited two distinct peaks corresponding to separate relaxation processes.

A simple, commonly-used R-C parallel model was tested, Fig. 5c, inset. This model typically describes the charge transfer and diffusion processes in electrode materials.[18] Here, the resistor (R) represents the impedance to current flow, while the capacitor (C) arises from the polarisation capacitance within the material structure. Considering the potential roughness or non-uniform charge distribution on the electrode surface, a constant phase element (CPE) was introduced as a replacer of the ideal capacitor. This two R-CPE parallel model was then used in series to simulate the grain boundary and bulk responses. R1-CPE1 and R2-CPE2 were assigned to the low-frequency and high-frequency semicircles in the impedance data, respectively.

The curves of both materials at various temperatures were fitted, and representative fitting results for NTO and R-NTO at 150 °C ($1000/T = 2.36\ K^{-1}$) are shown in Fig. 5c. Notably, in the low-frequency region of NTO, an upward-sloping trend appears, which may indicate Warburg impedance, suggestive of the diffusion-controlled behaviour in the electrochemical system. This diffusion slope was only observed at high temperatures due to the increase in ion diffusion rate, the reduction in diffusion time constant, and the resulting shift of the characteristic frequency into the measurement range. Furthermore, at elevated temperatures, the reduction in interfacial impedance makes the diffusion process more prominent. To better fit the obtained data, a Warburg impedance element (Wo) was included into the fitting model, as shown in Fig. 5c, however, within the frequency range used, only a limited Warburg spike was observed. As a result, this element was only included for the fit in the data set where this was clearly observed.

The activation energies were determined to be 456 meV for NTO and 321 meV for R-NTO as shown in Fig. 5d. This demonstrates that R-NTO has a lower activation energy vs NTO, reducing the energy barriers for electron and ion transport, enabling more efficient ion diffusion and charge transfer during charge-discharge processes.[35,36] It should be noted that in the lower temperature region of the plot (above the dotted line on the plot at 50 °C) the activation energy in both samples shows a different gradient, indicating a reduction in activation energy (c. 250 meV and 170 meV for the non-reduced and reduced NTO respectively). The activation of both samples decrease by roughly a factor of two in the low temperature area, which indicates that this effect is highly likely to be intrinsic to $Na_2Ti_3O_7$ rather than arising as a result of reduction. The low temperature regime is important to consider, however, as this is the temperature regime within which an Na-ion battery might be expected to operate. Previous research[16] has observed a similar effect, and through systematic study of atmosphere and heating history, established that both of these factors, and the likely presence of adsorbed water.

At high current densities, materials with lower activation energy can achieve faster charge transport, enabling high rate capability during rapid charge-discharge cycles.[37] This explains the enhanced cycling stability of R-NTO compared to NTO under varying C rates (Fig. 3b), as more efficient ion migration helps reduce localised stress and material degradation, ultimately extending battery lifespan.[38,39]

The bulk electronic conductivity, derived from the fitting results and geometric factors, was plotted as Arrhenius plots for NTO and R-NTO at different temperatures in Fig. 5d. At room temperature (25 °C), the conductivity of NTO is 9.7×10^{-8} S.cm^{-1}, which is consistent with values reported previously.[16] In contrast, RNTO exhibits a significantly higher conductivity of 4.0×10^{-7} S.cm^{-1}. This nearly fourfold increase confirms that the reduction treatment effectively enhances the electronic transport properties of the material, in line with the electrons liberated in Eq. 1.

This size of the increase in conductivity is in line with previous studies,[23] and we therefore attribute the enhancement of conductivity in $Na_2Ti_3O_7$ to the formation of Ti^{3+}, primarily due to its unique $3d^1$ electronic configuration, as opposed to the $3d^0$ configuration of Ti^{4+}, which lacks free electrons. Additionally, the formation of oxygen vacancies during the reduction process further contributes by creating additional pathways for electron hopping.[19] At the same time, activation energy represents the energy barrier for charge transfer and ion diffusion. In R-NTO, the introduction of Ti^{3+} and the formation of oxygen vacancies significantly lower this barrier. The mixed electronic states brought about by Ti^{3+} facilitate more efficient electron transport, while oxygen vacancies enhance ion migration dynamics. A reduced activation energy allows for smoother sodium-ion movement within the material, particularly under high-rate charge-discharge conditions, effectively minimising charge accumulation and localised chemical stress. The reduction process does not significantly disrupt the original crystal structure of $Na_2Ti_3O_7$ but alters the oxidation state to induce subtle structural adjustments that substantially improve conductivity and stability. The increases in specific capacity and cycle stability observed are therefore likely to be a combined effect of increased ion channel width and changes to the conductivity. This reduction strategy offers a simple and efficient approach to optimising Na-ion battery anode materials. By carefully controlling reduction conditions, the generation of electrons and oxygen vacancies can be maximised to enhance the material's electrochemical properties.

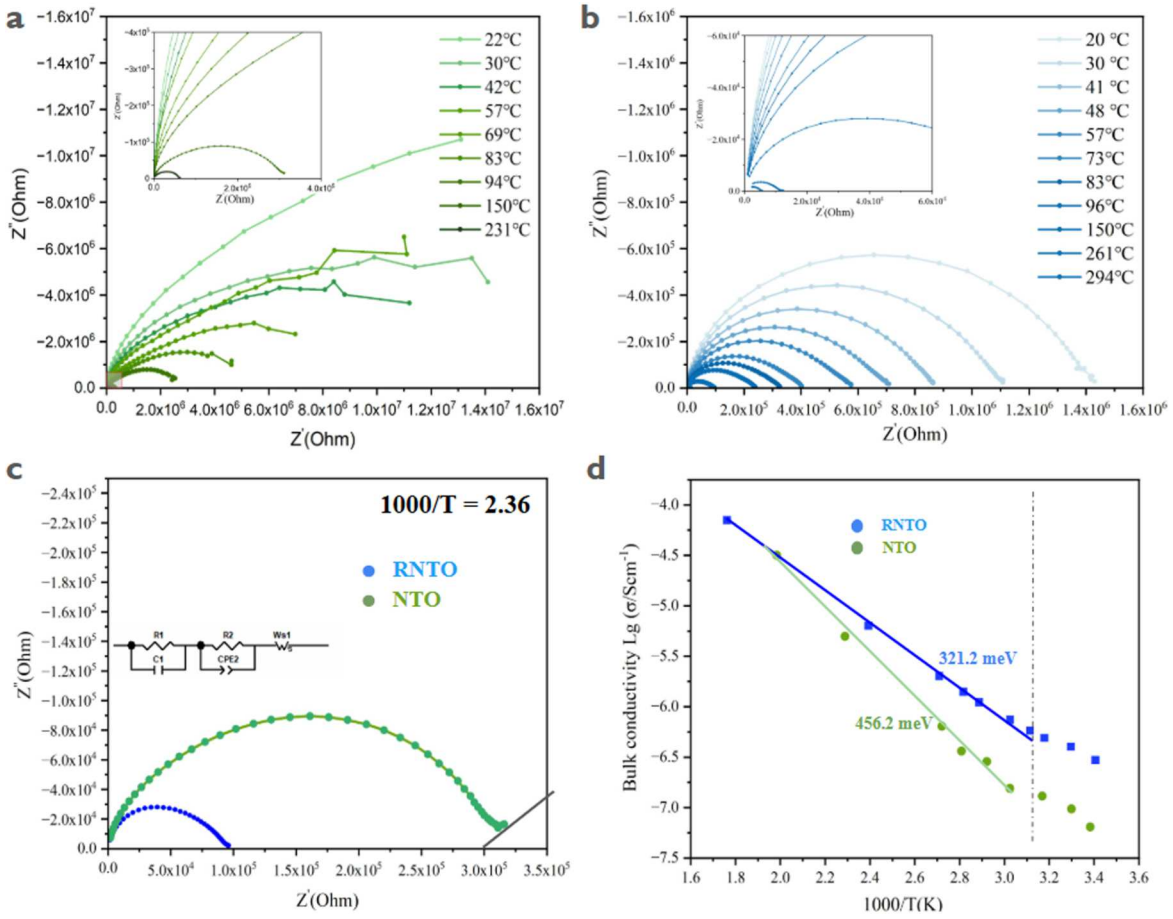

Figure 5. Z'-Z' plots of (a) NTO and (b) R-NTO at a range of temperatures, with (c) an example of data used to model the equivalence circuit (inset), including the modelled Warburg spike. The Arrhenius plot of NTO (green) and R-NTO (blue) is shown in (d), along with the fitted activation energies.

Conclusions

In conclusion, we have demonstrated that synthesis of $Na_2Ti_3O_7$ in a reducing environment can be used to improve both specific capacity and rate capability. By using a H_2/N_2 reducing environment, Ti^{3+} ions are generated, as indicated by a change in colour and lattice parameters. This reduction creates additional electrons and increases the total room temperature conductivity significantly, alongside an increase in lattice parameters which acts to increase Na-ion channel width. These factors in combination lead to the observed increase in specific capacity due to easier Na ion migration. The enhanced conductivity and observed decrease in activation energy leads to improved rate capability in R-NTO, which arises due to enhanced charge transfer rates. Overall, this work provides a straightforward method to improve across key electrochemical performance metrics in $Na_2Ti_3O_7$.

Acknowledgments

YL would like to acknowledge Mr Renjie Liu and Dr Stephanie Mudd for their advice on approach to data analysis. RB and PK acknowledge the Faraday Institution NEXGENNa project (FIRG018) for funding. All authors acknowledge support from the Henry Royce Institute, funded through EPSRC grants EP/R00661X/1, EP/S019367/1, EP/P02470X/1 and EP/P025285/1, for access to the X-ray diffraction facility, and the Royce Small Equipment Fund for the battery assembly facilities. The authors thank the Sorby Centre for Electron Microscopy for the SEM imaging. Authors also wish to thank the battery lab at Kroto Research Institute and the Henry Royce Institute for the opportunity to run measurements in the Maccor Series 4300 battery cycler. RB acknowledges the EPSRC Core Capital scheme for funding for the temperature-controlled chamber.

Author Contributions

YL conducted the experimental work, and performed data analysis. PK supported data collection and analysis. RB and YL designed the study, and wrote the manuscript. All authors edited the manuscript. RB obtained grants to support the research.

ORCID

Yining Li https://orcid.org/0009-0007-4796-7891
Pooja Kumari https://orcid.org/0000-0002-8461-1305
Rebecca Boston https://orcid.org/0000-0002-2131-2236

References

1. N. Tapia-ruiz et al., *J. Phys.: Energy*, **3**, 031503 (2021).
2. Y. Li, L. Mu, Y.-S. Hu, H. Li, L. Chen, and X. Huang, *Energy Storage Mater.*, **2**, 139 (2016).
3. Y. Li, S. Xu, X. Wu, J. Yu, Y. Wang, Y.-S. Hu, H. Li, L. Chen, and X. Huang, *J. Mater. Chem. A*, **3**, 71 (2015).
4. X. Chen, Y. Zheng, W. Lui, C. Zhang, and J. Li, *Nanoscale*, **11**, 22196 (2019).
5. S.-M. Zheng, Y.-R. Tian, Y.-X. Liu, S. Wang, C.-Q. Hu, B. Wang, and K.-M. Wang, *Rare Met.*, **40**, 272 (2021).
6. X. Nie, Z. Chen, B. Deng, L. Shao, J. Xu, X. Shi, and Z. Sun, *Adv. Energ. Mater.*, **15**, 2500069 (2025).
7. F. Chen, H. Li, Z. Qiao, R. Wang, C. Hu, T. Chen, Y. Niu, B. Zhong, Z. Wu, and Z. Guo, *Chinese J. Chem. Eng.*, **72**, 226 (2024).
8. J. Dong, Y. Jiang, R. Wang, Q. Wei, Q. An, and X. Zhang, *J. Energy Chem.*, **88**, 446 (2024).
9. J. Xu, C. Ma, M. Balasubramanian, and Y. S. Meng, *Chem. Commun.*, **50**, 12564 (2014).
10. S. Altin, S. Demirel, E. Oz, E. Altin, C. Hetherington, A. Bayri, and S. Avci, *CrystEngComm*, **14**, 2483 (2020).
11. A. Rudola, K. Saravanan, S. Devaraj, H. Gong, and P. Balaya, *Chem. Commun.*, **49**, 7451 (2013).
12. P. Kumari, Y. Li, and R. Boston, *Nanoscale*, **15**, 12087 (2023).

13. C. Wu, W. Hua, Z. Zhang, B. Zhong, Z. Yang, G. Feng, Q. Xiang, Z. Wu, and X. Guo, *Adv. Sci.*, **5**, 1800519 (2018).
14. W. Wang, C. Yu, Z. Lin, J. Hou, H. Zhu, and S. Jiao, *Nanoscale*, **5**, 594 (2013).
15. S. Chandel, S. Lee, S. Lee, S. Kim, S. P. Singh, J. Lim, and A. K. Rai, *J. Electroanal. Chem.*, **877**, 114747 (2020).
16. Y. S. Choi, S. I. R. Costa, N. Tapia-Ruiz, and D. O. Scanlon, *ACS Appl. Energy Mater.*, **6**, 484 (2023).
17. A. L. Sauvet, S. Baliteau, C. Lopez, and P. Fabry, *J. Solid State Chem.*, **177**, 4508 (2004).
18. M. Dynarowska, J. Kotwiński, M. Leszczynska, M. Marzantowicz, and F. Krok, *Solid State Ionics*, **301**, 35 (2017).
19. Z. Lu, H. Zhang, W. Lei, D. C. Sinclair, and I. M. Reaney, *Chem. Mater.*, **28**, 925 (2016).
20. S. R. Mudd, Y. Zhu, E. C. Montesdeoca, J. Andrews, R. Freer, and R. Boston, *J. Eur. Ceram. Soc.*, **45**, 116901 (2024).
21. D. I. Woodward, I. M. Reaney, G. Y. Yang, E. C. Dickey, and C. A. Randall, *Appl. Phys. Lett.*, **84**, 4650 (2004).
22. R. Nawaz, C. F. Kait, H. Y. Chia, M. H. Isa, L. W. Huei, N. T. Sahrin, and N. Khan, *Surf. Interfaces*, **32**, 102146 (2022).
23. R. Boston, W. L. Schmidt, G. D. Lewin, A. C. Iyasara, Z. Lu, H. Zhang, D. C. Sinclair, and I. M. Reaney, *Chem. Mater.*, **29**, 265 (2017).
24. S. Hui and A. Petric, *J. Electrochem. Soc.*, **149**, J1 (2002).
25. J. Chen, Z. Ding, C. Wang, H. Hou, Y. Zhang, C. Wang, G. Zou, and X. Ji, *ACS Appl. Mater. Interfaces*, **8**, 9142 (2016).
26. Q. Gan, H. He, Y. Zhu, Z. Wang, N. Qin, S. Gu, Z. Li, W. Luo, and Z. Lu, *ACS Nano*, **13**, 9247 (2019).
27. W. Meng, Z. Dang, D. Li, and L. Jiang, *Adv. Mater.*, **35**, 1 (2023).
28. T. Song, S. Ye, H. Liu, and Y. G. Wang, *J. Alloys Compd.*, **767**, 820 (2018).
29. B. H. Toby and R. B. Von Dreele, *J. Appl. Crystallogr.*, **46**, 544 (2013).
30. H. Pan et al., *Adv. Energy Mater.*, **3**, 1186 (2013).
31. S. Chen, L. Gao, L. Zhang, and X. Yang, *Ionics*, **25**, 2211 (2019).
32. F. Su, K. Dai, Y. Kang, M. Shui, and L. Shu, *Ionics*, **29**, 4001 (2023).
33. J. Hwang, H. S. Cahyadi, W. Chang, and J. Kim, *J. Supercrit. Fluids*, **148**, 116 (2019).
34. J. T. S. Irvine, D. C. Sinclair, and A. R. West, *Adv. Mater.*, **2**, 132 (1990).
35. M. Wu, W. Ni, J. Hu, and J. Ma, *Nano-Micro Letters*, **11**, 44 (2019).
36. P. Scheiber, M. Fidler, O. Dulub, M. Schmid, U. Diebold, W. Hou, U. Aschauer, and A. Selloni, *Phys. Rev. Lett.*, **109**, 1 (2012).
37. C. Heubner, K. Nikolowski, S. Reuber, M. Schnieder, M. Wolter, and A. Michaelis, *Batter. Supercaps*, **4**, 268 (2021).
38. A. Chanda, D. P. Abraham, S. E. Trask, and S. P. V. Nadimpalli, *EES Batter.*, **1**, 833 (2025).
39. J. S. Menye, M. B. Camara, and B. Dakyo, *Energies*, **18**, 342 (2025).